

See discussions, stats, and author profiles for this publication at: <https://www.researchgate.net/publication/310763807>

Metalated graphene nanoplatelets and their uses as anode materials for lithium-ion batteries

Article in *2D Materials* · November 2016

DOI: 10.1088/2053-1583/4/1/014002

CITATIONS

0

READS

69

8 authors, including:



Jiantie Xu

Case Western Reserve University

34 PUBLICATIONS 487 CITATIONS

SEE PROFILE



In-Yup Jeon

Ulsan National Institute of Science and Tech...

62 PUBLICATIONS 1,573 CITATIONS

SEE PROFILE



Jong-Beom Baek

Ulsan National Institute of Science and Tech...

235 PUBLICATIONS 7,654 CITATIONS

SEE PROFILE

All content following this page was uploaded by [Jiantie Xu](#) on 09 December 2016.

The user has requested enhancement of the downloaded file.

Metalated graphene nanoplatelets and their uses as anode materials for lithium-ion batteries

This content has been downloaded from IOPscience. Please scroll down to see the full text.

2017 2D Mater. 4 014002

(<http://iopscience.iop.org/2053-1583/4/1/014002>)

View [the table of contents for this issue](#), or go to the [journal homepage](#) for more

Download details:

IP Address: 203.10.91.73

This content was downloaded on 21/11/2016 at 00:06

Please note that [terms and conditions apply](#).

You may also be interested in:

[Freeze-drying for sustainable synthesis of nitrogen doped porous carbon cryogel with enhanced supercapacitor and lithium ion storage performance](#)

Zheng Ling, Chang Yu, Xiaoming Fan et al.

[Nitrogen-rich graphene from small molecules as high performance anode material](#)

Weiwei Gao, Hao Huang, Hongyan Shi et al.

[Vertically oriented MoS₂ nanoflakes coated on 3D carbon nanotubes for next generation Li-ion batteries](#)

Mumukshu D Patel, Eunho Cha, Nitin Choudhary et al.

[Free standing SnS₂ nanosheets on 3D graphene foam: an outstanding hybrid nanostructure anode for Li-ion batteries](#)

Zhi Xiang Huang, Ye Wang, Jen It Wong et al.

[Carbon-decorated Li₄Ti₅O₁₂/rutile TiO₂ mesoporous microspheres with nanostructures as high-performance anode material in lithium-ion batteries](#)

Lin Gao, Rujun Liu, Hao Hu et al.

2D Materials



PAPER

Metalated graphene nanoplatelets and their uses as anode materials for lithium-ion batteries

RECEIVED
30 September 2016

REVISED
27 October 2016

ACCEPTED FOR PUBLICATION
2 November 2016

PUBLISHED
17 November 2016

Jiantie Xu^{1,4}, In-Yup Jeon^{2,4}, Hyun-Jung Choi², Seok-Jin Kim², Sun-Hee Shin², Noejung Park³, Liming Dai¹ and Jong-Beom Baek²

¹ Department of Macromolecular Science and Engineering, Case Western Reserve University, Cleveland, OH 44106, USA

² School of Energy and Chemical Engineering/Center for Dimension-Controllable Organic Frameworks, Ulsan National Institute of Science and Technology (UNIST), UNIST 50, Ulsan 44919, Korea

³ School of Natural Science, Ulsan National Institute of Science and Technology (UNIST), UNIST 50, Ulsan 44919, Korea

⁴ These authors contributed equally.

E-mail: jbbaek@unist.ac.kr, noejung@unist.ac.kr and liming.dai@case.edu

Keywords: metalation, ball-milling, graphene nanoplatelets, anode materials, lithium-ion batteries

Supplementary material for this article is available [online](#)

Abstract

A series of post-transition metals and semimetals in groups IIIA (Al, Ga, In), IVA (Ge, Sn, Pb) and VA (As, Sb, Bi) were introduced onto graphene nanoplatelets (GnPs) by mechanochemical reaction. The selected metals have a lower electronegativity (χ , $1.61 \leq \chi_M \leq 2.18$) but a much larger covalent atomic radius ($d_M = 120\text{--}175$ pm) than carbon ($\chi_C = 2.55$, $d_C = 77$ pm). The effect of the electronegativity and atomic radius of the metalated GnPs (MGnPs, M = Al, Ga, In, Ge, Sn, Pb, As, Sb, or Bi) on the anode performance of lithium-ion batteries was evaluated. Among the series of prepared MGnPs, GaGnP ($\chi_{Ga} = 1.81$, $d_{Ga} = 135$ pm) in group IIIA, SnGnP ($\chi_{Sn} = 1.96$, $d_{Sn} = 140$ pm) in group IVA and SbGnP ($\chi_{Sb} = 2.05$, $d_{Sb} = 141$ pm) in group VA exhibited significantly enhanced performance, including higher capacity, rate capability and initial Coulombic efficiency. Both the experimental results and theoretical calculations indicated that the optimum atomic size ($d_M \sim 140$ pm) was more significant to the anode performance than electronegativity, allowing not only efficient electrolyte penetration but also fast electron and ion transport across the graphitic layers.

1. Introduction

Today, lithium-ion batteries (LIBs) not only dominate the market in electronic devices (e.g., MP3, PC, camera), they have become one of the most promising rechargeable energy sources for electric vehicles (EV) and hybrid EV (HEV) [1]. However, to meet the ever-increasing demand for EVs and HEVs, and provide sufficiently high energy and power densities, it is critically necessary to explore and develop LIB electrode materials [2, 3]. Over the past few decades, many efforts have been devoted to developing anode materials for LIBs, which can replace commercial graphite, which has low theoretical capacity of 372 mAh g^{-1} and poor rate capability. The search for alternatives has involved the study of $\text{Li}_4\text{Ti}_5\text{O}_{12}$, Si, Sn, metal oxides, and graphene [4]. Among these alternatives, graphene has proved to be an ideal new anode material for LIBs,

with much higher capacity and rate capability than graphite [5]. Graphene's excellent electrochemical performance can be attributed to its particular combination of properties, including electrical conductivity, large surface area, remarkable mechanical flexibility and thermal stability [6].

Significant efforts have been made to further enhance the anode performance of graphene-based materials by controlling their morphology (e.g., disordering their surface morphology, porosity, creating holes and defects) [5, 7–22] and by introducing heteroatoms or heteroatom-containing functional groups (e.g., B, N, S, P, F, Cl, Br, I, or combinations thereof) [9, 13, 17, 18, 23–34]. When lithium intercalates into graphite, lithium ions diffuse mainly in the in-plane direction, and then the ions occupy sites between two adjacent graphitic planes. When the graphite is in a fully lithiated state, each lithium is

associated with a hexagonally connected graphitic carbon (C) to form a Li–C₆–Li–C₆ sequence along the *c*-axis [35–37]. Because of this process, the graphitic edges play a key role during the lithiation–delithiation, by providing active sites/portals for lithium ion storage/diffusion into internal graphitic layers [38].

Recently, we prepared a series of edge-halogenated graphene nanoplatelets (XGnPs, X = F, Cl, Br, I, COOH or H) by ball-milling graphite in the presence of fluorine (F₂), chlorine (Cl₂), bromine (Br₂), iodine (I₂), carbon dioxide (CO₂) or hydrogen (H₂). These XGnPs displayed good electrochemical performance with cycle stability suitable for use in LIBs [27, 33]. The enhanced electrochemical performance of XGnPs is attributable to the combination of higher electronegativity and widened graphitic edges, which can support efficient lithiation–delithiation. One of features of halogens (X = Cl, Br and I) is that they have a higher electronegativity ($\chi = 2.66$ – 3.16) and larger atomic radius ($d_X = 99$ – 133 pm) than carbon ($\chi_C = 2.55$, $d_C = 77$ pm). To date, while intensive studies have been carried out to verify the positive effect of polar heteroatom-doped carbon based materials on anodic performance for LIBs, their effect on the interlayer distance (*d*)–(*d*) of graphitic edges has still not been clarified. Given the nature of graphitic anodes, understanding this edge effect is a critically important step toward designing a new class of anode materials for high capacity LIBs with stable cycling.

2. Experimental section

2.1. Materials

MGnPs were prepared by ball-milling graphite (Alfa Aesar, Natural, –100 mesh, 99.9995% metals basis, #14735) in the presence of post-transition metal (M = Al, Ga, In, Sn, Pb or Bi) or semimetal (M = Ge, As or Sb) in a planetary ball-mill crusher. In a typical experimental set-up, graphite (5.0 g) and M (5.0 g) were placed in a stainless steel container (250 ml). After adding 500 g of stainless steel balls, the container was sealed and five cycles of argon charging (70 psi)/discharging (0.05 mm Hg) were applied to remove air completely. The container was then fixed in a planetary ball-mill machine and agitated at 500 rpm for 48 h. The resultant MGnPs were treated with 1.0 M aq. HCl solution for 48 h to etch off residual free-standing metallic reactants and impurities and further treated with warm concentrated HCl (~37%), concentrated HNO₃ (~70%), or aqua regia (HNO₃ + 3 HCl) to remove the remaining reactants (post-transition metal or semimetal). The solid samples collected by filtration were freeze-dried at –120 °C under reduced pressure (0.05 mm Hg) for 48 h, to yield dark black MGnPs. The reference materials, hydrogenated GnPs (HGnP) and carboxylated GnP (CGnP), were prepared using very similar procedures to those applied for MGnPs, except for the gas charging [39].

2.2. Instrumentation

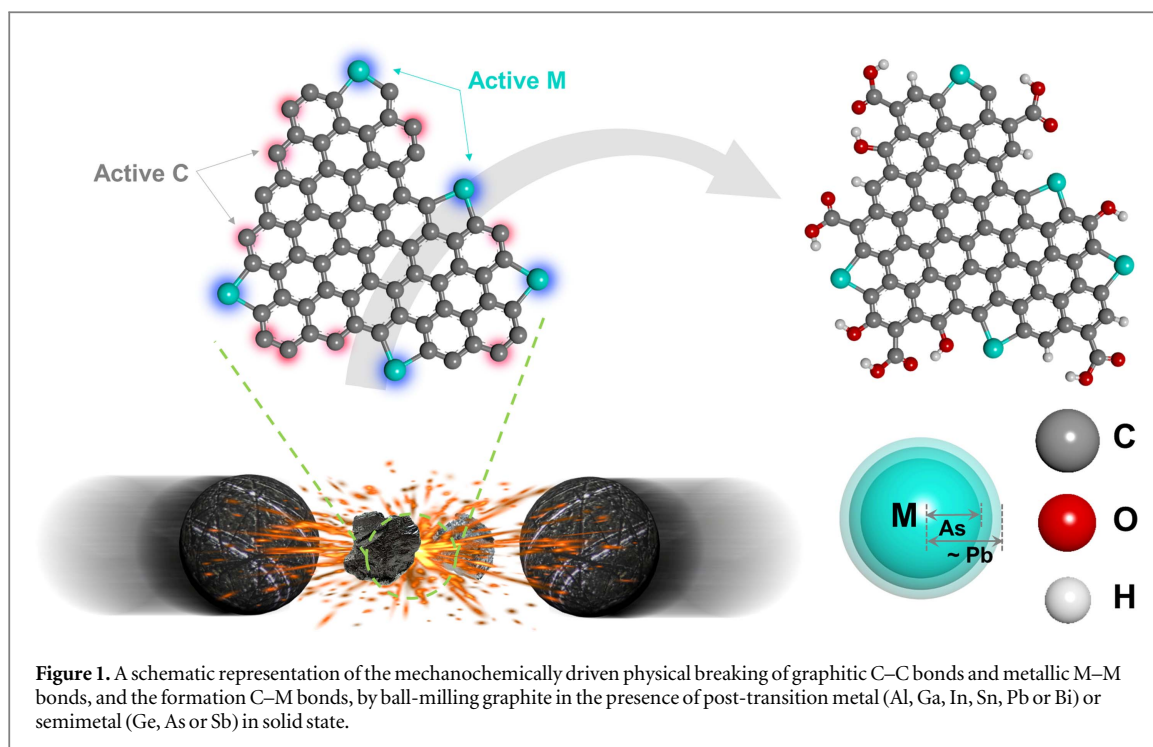
The field emission scanning electron microscopy (FE-SEM) was performed using an FEI Nanonova 230. Atomic resolution transmission electron microscopy (AR-TEM) was carried out on a Titan G2 Cube 60–300 microscope. Time-of-flight secondary ion mass spectrometry (TOF-SIMS) was carried out with a TOF-SIMS V instrument (ION-TOF GmbH, Germany) using a 10 keV Bi⁺ primary ion-beam source. X-ray photoelectron spectra (XPS) were recorded on a Thermo Fisher K-alpha XPS spectrometer. The surface area was measured using nitrogen adsorption/desorption isotherms using the Brunauer–Emmett–Teller (BET) method on a Micromeritics ASAP 2504 N. Thermogravimetric analysis was conducted on a TA Q200 (TA Instrument) at a heating rate of 10 °C min^{–1} under air.

2.3. Electrochemical analysis

The electrochemical characterization of all the samples was carried out using coin cells. The two-electrode electrochemical cells were fabricated by blending the active materials with acetylene black carbon and PVDF, at a weight ratio of 8:1:1, respectively. *N*-methyl-2-pyrrolidone (NMP) was used as the blending solvent for the mixture. The obtained slurry was coated on Cu foil, dried at 90 °C for 12 h, and pressed at 2 MPa. *N*-methyl-2-pyrrolidone (NMP) was used as the blending solvent for the mixture. The electrode was punched from as-prepared electrode paper in a round disk and the mass loading of an electrode was controlled to ~3 mg cm^{–2}. CR 2032 coin-type cells were assembled in an Ar-filled glove box using the as-prepared electrode as the working electrode, lithium foil as the counter electrode and reference electrode, porous polypropylene film as separator, and 1 M LiPF₆ (Sigma-Aldrich) in a 1:1:1 (v/v/v) mixture of dimethyl carbonate, ethylene carbonate, and diethyl carbonate as the electrolyte. The cells were galvanostatically charged and discharged using an automatic battery tester system (Land®, China) at various current densities in the range 0.02–3 V (assumption: 1 C = 500 mA g^{–1}). It should be noted that, given the various theoretical capacities of MGnPs, for simple description the normalized current density (C) in 1 h for all MGnPs was assumed to be 500 mA g^{–1}. Electrochemical impedance spectroscopy (EIS) measurements were performed using a computer-controlled potentiostat (CHI 760 C, CH Instruments, USA). Impedance plots were collected for the cells from 10⁵ Hz to 10 mHz. The cyclic voltammograms (CV) and EIS were measured using a Biologic VPM3 electrochemical workstation.

2.4. *Ab initio* calculation method

For computations, we used the Vienna *Ab initio* Simulation Package to calculate the ground state of a many-electrons system in the frame work of density



functional theory (DFT) [40–43]. The plane-wave basis set, with an energy cut-off of 400 eV, and the gradient-corrected exchange-correlation potential suggested by Perdew, Burke, and Ernzerhof (PBE-type), were employed [44].

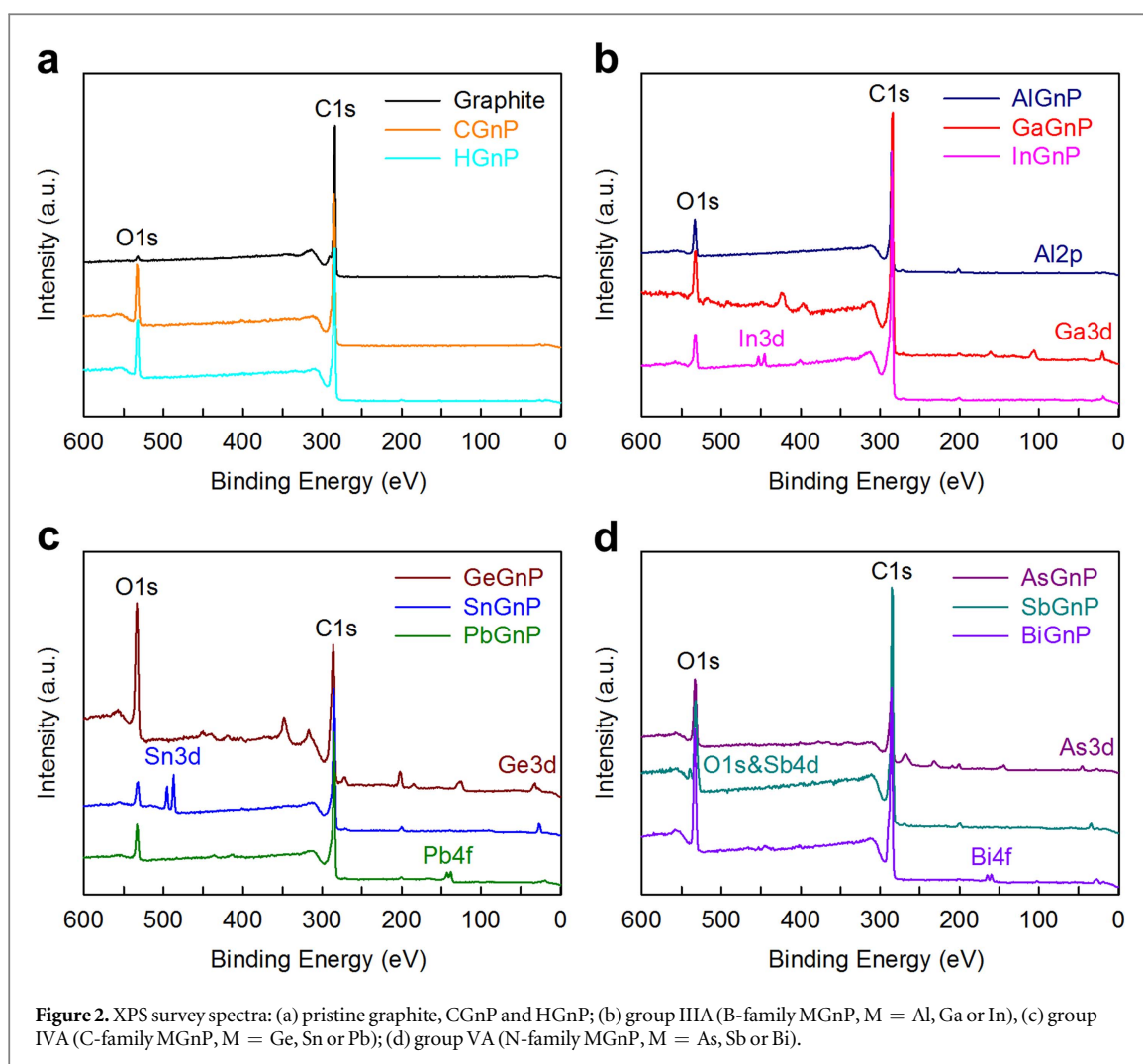
3. Results and discussion

To clarify how the effect of graphitic edges can minimize the contribution of electronegativity, a series of metalated GnPs (MGnPs, M = Al, Ga, In, Ge, Sn, Pb, As, Sb or Bi) were, for the first time, systematically introduced by a mechanochemical reaction driven by the ball-milling technique. As schematically represented in figure 1, post-transition metal (Al, Ga, In, Sn, Pb or Bi) or semimetal (Ge, As or Sb)-functionalized graphene nanoplatelets (MGnPs, M = Al, Ga, In, Ge, Sn, Pb, As, Sb or Bi) were prepared simply by dry ball-milling graphite in the presence of the corresponding metal (details are described in the Experimental section). The metal (M) atoms in the MGnPs have a larger atomic size (covalent radius, $d_M = 120\text{--}175\text{ pm}$) (figure S1), but a much lower electronegativity ($\chi_M = 1.67\text{--}2.05$) than carbon atoms ($d_C = 77\text{ pm}$, $\chi_C = 2.55$). For further comparison, (HGnP, $d_H = 37\text{ pm}$, $\chi_H = 2.20$) and CGnP were also prepared by ball-milling graphite in the presence of hydrogen (H_2) and dry ice (solid CO_2), respectively.

SEM images of graphite before and after ball-milling in the presence of the corresponding metals illustrate the dramatic changes in grain sizes produced by the milling (figure S2). While the pristine graphite has a flake-type morphology with large grain size

(<150 μm , figure S2(a)), the dimensions of all the prepared MGnPs were dramatically reduced (<1 μm , figures S2(b)–S2(l)), which confirms that mechanochemical reactions occurred. After a complete work-up to remove unreacted metals and other impurities (as described in Experimental section), the presence of the essential elements was clearly observed in the MGnPs by SEM energy dispersive x-ray spectroscopy (EDS) (figure S3). The corresponding elemental contents were in the range of approximately 0.44–19.27 at% (table S1). Furthermore, high resolution transmission microscopy (HR-TEM) and atomic-resolution TEM (AR-TEM) with scanning TEM (STEM) images of the prepared AlGnP showed that the Al element in the AlGnP had atomic level distribution rather than forming a bulk solid state aggregated cluster (figure S4). In accordance with our previous reports [45, 46], these results provide evidence that carbon (C) and metal (M) bonds were formed as a result of mechanochemical reactions during the ball-milling.

XPS analysis has been widely utilized to identify the chemical bonding and/or heteroatom-doping level of carbon materials [27–30]. Pristine graphite exhibits a major C 1s peak from the sp^2 C–C bond, along with a minor O 1s peak, due to physical absorption of oxygen and moisture (figure 2) [47]. The MGnPs display characteristic peaks for each element (Al 2p, Ga 3d, In 3d, Ge 3d, Sn 3d, Pb 4f, As 3d, Sb 4d or Bi 4f) [45, 47–57], in addition to the main C 1s peak along with relatively stronger O 1s peaks. The presence of the O 1s peak(s) in each sample is due to termination reactions of the remnant active carbon species upon contact with air moisture (i.e., O_2 , CO_2 and H_2O) upon exposing the sample after processing.



As determined by XPS, the content of ‘M’ elements in the MGnPs were in the range 0.15–3.74 at% (table S2). The large discrepancy between the SEM EDS and XPS results is due to the difference between the two methods. It is generally appreciated that XPS significantly underestimates metallic elements [58, 59]. In addition, the formation of C–M bonds could be confirmed by exemplary HR XPS spectra of MGnPs (figure S5). Deconvoluted XPS spectra of Bi 4f (figure S5(a)), In 3d (figure S5(b)) and Pb 4f (figure S5(c)) suggest the formation of C–M bonds.

To further verify the formation of C–M bonds in the MGnPs, pristine graphite and each type of MGnPs were compared one-by-one using TOF-SIMS. The positive ion spectra of the MGnPs show the presence of ions as the isotopes of each element (M = Al, Ga, In, Ge, Sn, Pb, As, Sb or Bi) (figure 3), while pristine graphite shows only the hydrocarbon peak, without any peaks related to post-transition metals or semimetals.

The Raman spectra for all of the MGnPs showed a D band at around 1350 cm^{-1} and a G band at around 1560 cm^{-1} (figure S6). The ratios of the D- to G-band intensities (I_D/I_G) of the MGnPs are in the range of 0.83–1.04, due to significant edge contributions caused

by the reduction in grain size ($<1\ \mu\text{m}$, see figure S2) and metalation. The specific surface areas of the MGnPs were determined by BET plots of an N_2 adsorption isotherm (table S3). All of the MGnPs showed much higher specific surface areas ($117\text{--}463\text{ m}^2\text{ g}^{-1}$) than pristine graphite ($2.8\text{ m}^2\text{ g}^{-1}$) [47]. This indicates that the MGnPs had been significantly exfoliated into a few graphitic layers (average number of layers = $2630\text{ m}^2\text{ g}^{-1}$, divided by the specific surface area of the MGnPs). In addition, the MGnPs exhibited a high pore volume ($0.18\text{--}0.46\text{ ml g}^{-1}$) and a mesoporous nature (pore size $< 5\text{ nm}$), which can contribute to electrochemical performance (*vide infra*).

Given this structural information, the MGnPs were then evaluated as anode materials for LIBs. The discharge/charge profiles of the MGnPs (M = H, C, Al, Ga, In, Ge, Sn, Pb, As, Sb or Bi) were measured at various C-rates from 0.1 to 10 C in the voltage range of 0.02–3 V, and the results are shown in figure 4 and S7, respectively. Together with the discharge/charge profiles of CGnP and HGnP (figures 4(a)–(c)), all of the other MGnPs show typical electrochemical behaviors of carbonaceous materials, which is in agreement with previous results [15, 22, 29, 31].

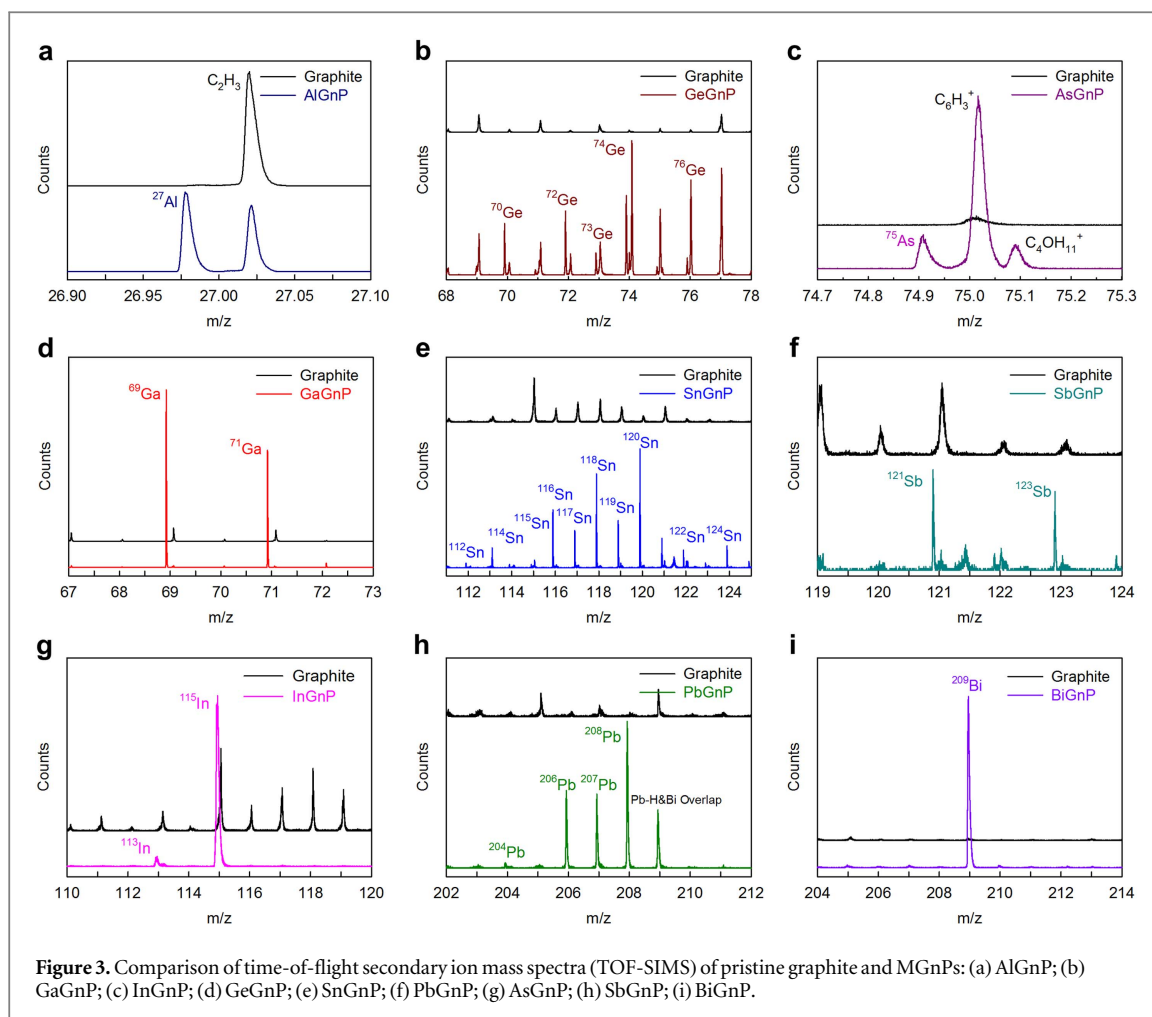


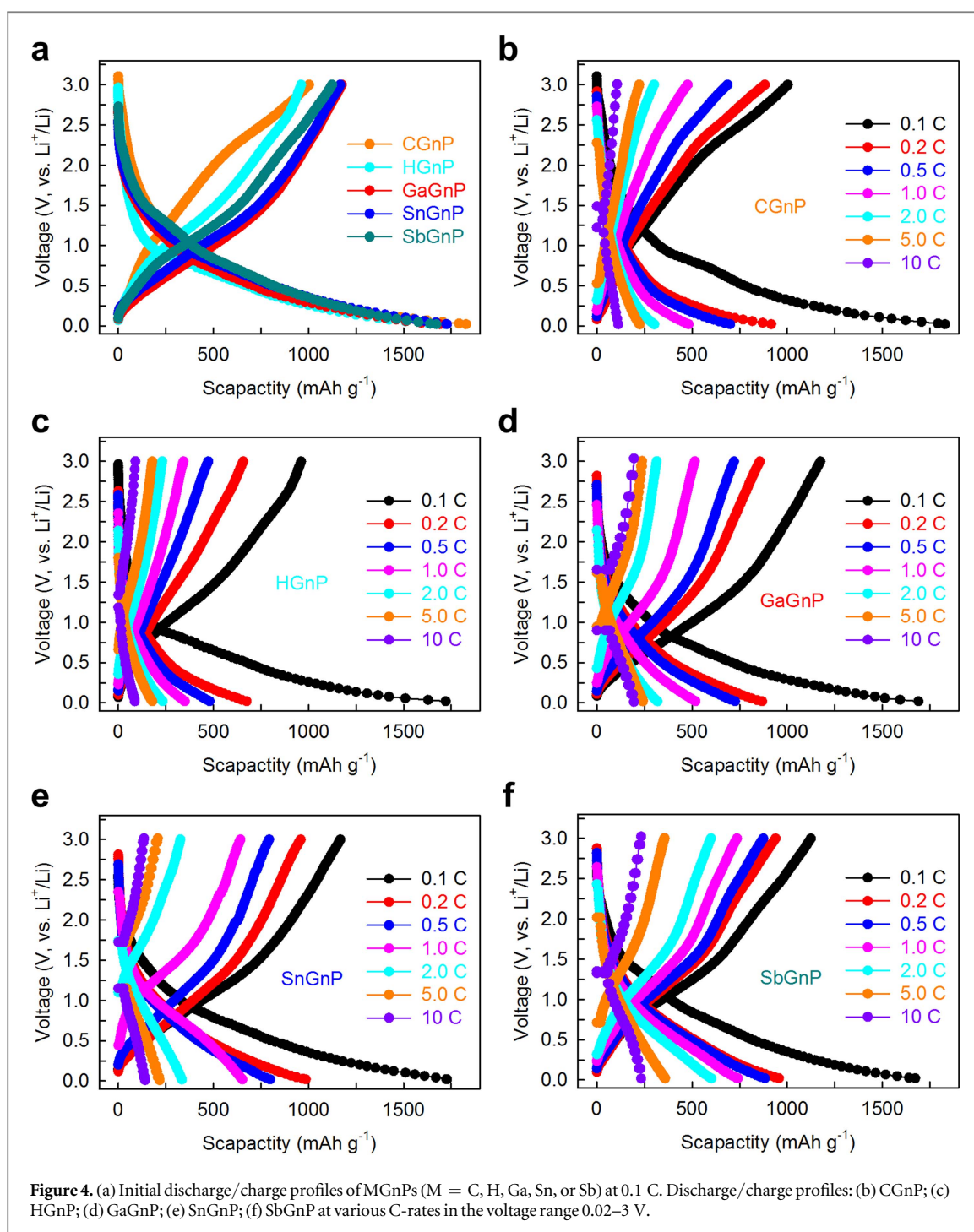
Figure 3. Comparison of time-of-flight secondary ion mass spectra (TOF-SIMS) of pristine graphite and MGnPs: (a) AlGnP; (b) GaGnP; (c) InGnP; (d) GeGnP; (e) SnGnP; (f) PbGnP; (g) AsGnP; (h) SbGnP; (i) BiGnP.

In the CV of the MGnPs ($M = C, H, Ga, Sn$ or Sb), the first cathodic peaks appear at around 0.9 V in the first cycle and then almost disappear in the following cycles, as measured during the initial three scans between 0.02 and 3 V at a scan rate of 0.2 mV s^{-1} (figure S8). This indicates the formation of a solid-electrolyte interphase (SEI) layer on the sample surfaces in the first cycle. After the formation of the SEI film, the starting cathodic peak at around 0.5 V is related to the insertion of Li^+ into the graphitic layers, which is a key indicator of lithium storage in graphene.

During anodic scans, the MGnPs ($M = Ga, Sn$ or Sb), and particularly, the SbGnP, clearly showed partially reversible redox peaks at around 0.5, 1, and 2.5 V, which are most likely due to the interaction between lithium ions and the defects/oxygen containing functional groups at the terminal ends of graphitic layers. This indicates that electroactivity was higher for the MGnPs ($M = Ga, Sn$ or Sb) than for HGnP and CGnP. Moreover, the high reversibility and stable structure of the MGnPs (e.g., $M = Sb$ and Ga) was also further confirmed by *ex situ* XRD. The mechanism of lithium ions stored in MGnPs was studied by XRD. As shown in figure S9, the *ex situ* XRD patterns of MGnPs (e.g., $M = Sb$ or Ga) at different discharge voltage of 2.7 V (open circuit voltage), 0.8 V (SEI formation), 0.02 V (full discharge) indicate various

degrees of lithium storage in the graphitic layers ([002] ‘peak left’ at $\sim 25^\circ$) during the discharge process. In the charge process, the [002] peak has a slight ‘right shift’ for MGnPs from 0.02 to 3.0 V (full charge) without any distinct impurity peaks, indicating the high reversibility and stable structure of MGnPs.

In order to investigate their rate and cycling performance, the MGnP cells were discharged and charged for 60 cycles between 0.02 and 3 V at various current rates (figure 5(a) and S10). In the periodic table, the M elements are divided into three different groups (Group IIIA: B-family, Group IVA: C-family, and Group V: N-family). As shown in figure S10, in the B-family, GaGnP exhibited a higher initial capacity (1689 mAh g^{-1}) than AlGnP ($882.15 \text{ mAh g}^{-1}$) and InGnP ($1159.44 \text{ mAh g}^{-1}$) at 0.1 C. The reference samples of CGnP had a higher initial discharge capacity ($1828.3 \text{ mAh g}^{-1}$) than HGnP ($1720.08 \text{ mAh g}^{-1}$). This is because oxygenated groups (e.g., $-\text{COOH}$ and $-\text{OH}$) were richly present in the CGnP. The higher oxygen content (table S2, XPS) for CGnP, which resulted from ball-milling graphite in the presence of dry ice (the solid form of CO_2), can favor higher lithium adsorption during the initial discharge process. Compared to HGnP and CGnP, all B-family MGnPs ($M = Al, Ga$ or In) showed a lower initial discharge capacity. The decreased discharge capacity of these



MGnPs may be attributed to stable M^{3+} (e.g., Al^{3+}), which cannot be further oxidized but reduces the active sites available for lithium ions storage. Similar cases have also been observed in intensive works on inactive aluminum doped cathode materials, in which aluminum only stabilizes its own structure [60]. Despite the reduced capacity of some MGnPs ($M = \text{Al, Ga, or In}$), their Coulombic efficiencies (figure 5(b), 63.2% for InGnP and 69.5% for GaGnP) were much higher than the reference samples CGnP (54.9%) and HGnP (50.1%). In addition, the rate capabilities of AlGnP and GaGnP (figure 5(c) and S11a) were significantly enhanced. This is thought to be due to improved

charge-transfer kinetics associated with the greater d_M-d_M entry of lithium ions during diffusion, which occurs during the lithium insertion/extraction processes. It should be noted that the lowest Coulombic efficiency (28.5%) for InGnP (with the largest $d_{\text{In}}-d_{\text{In}}$, figure S1) is most likely related to the formation of extensive agglomerations (figure S2(f)), low In content (table S2), and large charge-transfer resistance. Even so, InGnP showed a higher initial capacity than AlGnP.

The charge transfer kinetics was further confirmed by EIS. Two of the MGnPs ($M = \text{Al or Ga}$) showed a lower charge resistance (diameter of semicircle of EIS spectra) [27] than CGnP, HGnP and InGnP (figure

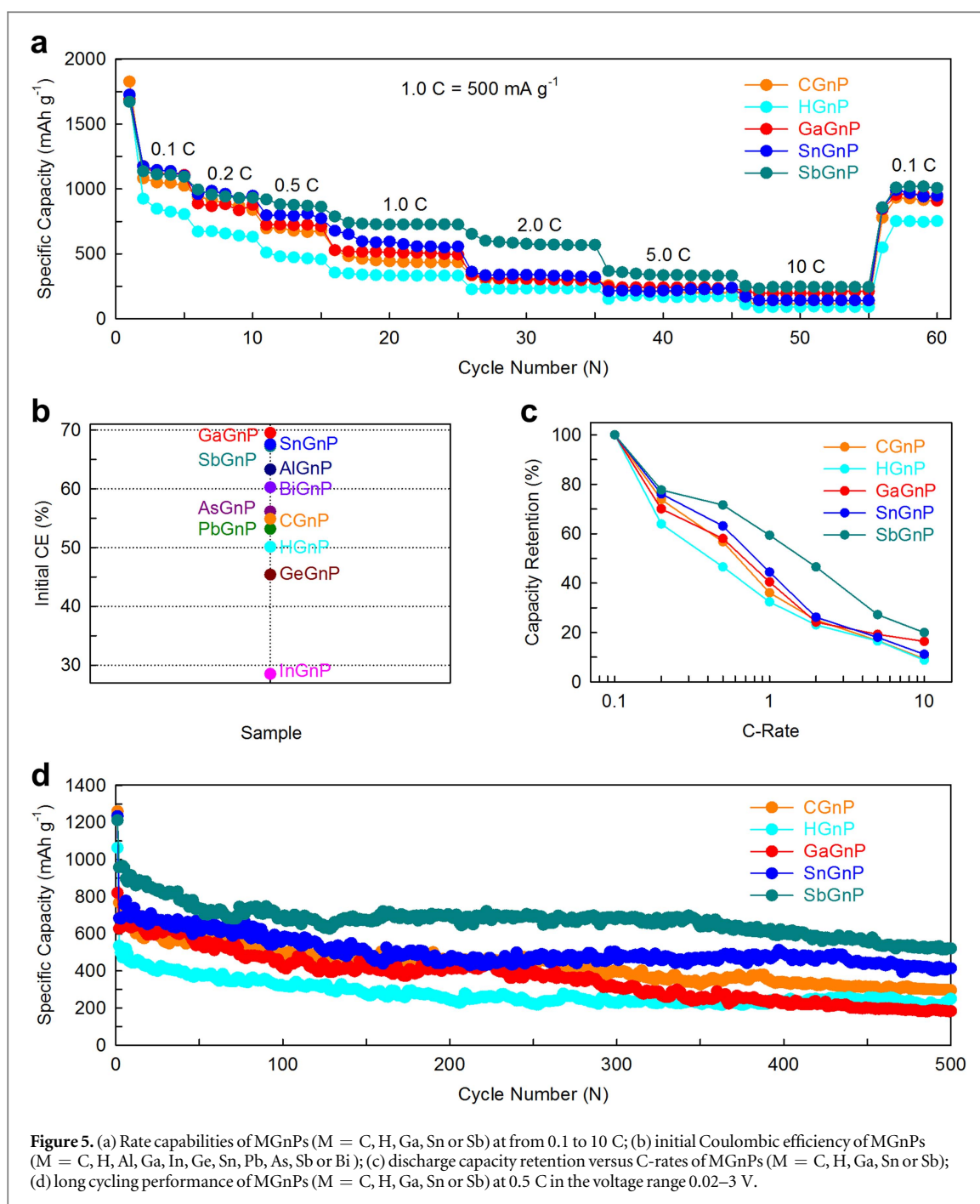


Figure 5. (a) Rate capabilities of MGnPs (M = C, H, Ga, Sn or Sb) at from 0.1 to 10 C; (b) initial Coulombic efficiency of MGnPs (M = C, H, Al, Ga, In, Ge, Sn, Pb, As, Sb or Bi); (c) discharge capacity retention versus C-rates of MGnPs (M = C, H, Ga, Sn or Sb); (d) long cycling performance of MGnPs (M = C, H, Ga, Sn or Sb) at 0.5 C in the voltage range 0.02–3 V.

S12(a)), indicating fast ion transport for AlGnP and GaGnP.

Compared to the transition metal M^{3+} in the B-family which had no higher oxidation states (Al, Ga and In); the M elements in the C-family (Ge, Sn and Pb) and the N-family (As, Sb and Bi) showed various oxidation states for many M or M-containing compounds [53]. This indicates potentially strong interactions between the C–OM or C–M groups and lithium ions. As shown in figure 5(a) and S10(b), the C-family MGnPs (M = Ge, Sn or Pb) exhibited the initial capacities of 1865.3, 1767.3, and 1727.45 mAh g⁻¹ at 0.1 C, with a Coulombic efficiency of 45.4, 67.7, and 53.2%, respectively. The N-family MGnPs (M = As, Sb or Bi) (figure 5(a) and S10(c)) exhibited initial capacities of

1905.7, 1671.8, and 1832.4 mAh g⁻¹, respectively, at 0.1 C; with a Coulombic efficiency of 56.1, 67.2 and 60.3%, respectively.

As can be seen, the initial capacities of the MGnPs (M = Ge or Sn) and MGnPs (M = As or Bi) were higher than those references CGnP (1828.3 mAh g⁻¹) and HGnP (1720.1 mAh g⁻¹). In addition, the higher initial Coulombic efficiencies of the MGnPs (M = Sn, Sb or Bi) as compared with the references (CGnP: 54.9%, HGnP: 50.1%) indicate the high reversibility of the lithium ion storage in the first cycle (figure 5(b)). The high initial CE is most likely related to strong interactions between lithium ions and C–OM or C–M at the termini, leading to the formation of a thin, strong SEI film and the fast, reversible diffusion of

lithium ions (*vide infra*). In a comparison of all the samples, SbGnP showed the best rate capability (figure 5(c), S11 and table S4). Consistent with its electrochemical performance, the lower charge-transfer resistance of SbGnP (among the MGnPs) was also confirmed by EIS measurements (figure S12).

To further compare their relatively long-term cycling performance, the MGnPs were measured at 0.5 C in the voltage range of 0.02–3 V for 500 cycles. The MGnPs exhibited the different cycling stability (figure 5(d) and S13) with different discharge capacities in the initial cycles and the 500th cycles (figure S14 and table 1). Generally, it was found that the best relatively long-term cycling stability occurred in AlGnP (AlGnP > GaGnP > InGnP), SnGnP (SnGnP > PbGnP > GeGnP) and SbGnP (SbGnP > BiGnP > AsGnP) in the B-, C- and N-families, respectively.

In combination with the results of the rate capability measurements for all MGnPs (figure 5(a) and table S4), the MGnPs (M = Ga, Sn and Sb) delivered the best electrochemical performance in each family compared to the references HGnP and CGnP. Coincidentally, the electronegativity (χ) and atomic size (d) of the M's were approximately 2.0 and 140 pm, which could also be associated with the high surface area, the optimum d_M-d_M , the moderate oxygenated groups, the low SEI resistance and the low charge transfer resistance.

Furthermore, SbGnP showed a higher reversible capacity over 500 cycles, than all the other MGnPs (figure 5(d)). To further investigate the kinetics of MGnPs, we also measured EIS for MGnPs (e.g., M = Ga, Sn, Sb or C) at 0.5 C at different cycles. As can be seen, the R_{ct} 's of MGnPs decrease from the 0th cycle to the 25th cycle (Figure S15). The decrease in R_{ct} is mainly attributed to the electrode–electrolyte activation, leading to the enhanced ionic conductivity and efficient utilization of active sites of electrode materials. Then, along with R_s , R_{ct} almost remain constant at 100th and 200th cycles, indicating the formation of strong SEI film and stable diffusion of lithium ions in the deep cycles. The observed kinetics of MGnPs as anode materials for LIBs is in agreement with the change trend of cycling performance. In spite of the different capacities and capacity retention, the average Coulombic efficiency of all the MGnPs approached 99% at 0.5 C (figure S16), indicating that the MGnPs maintain their structural integrity during the lithium ion insertion/extraction process.

Previously, we also reported excellent electrochemical results for fluorinated GnP (FGnP) as an LIB anode material, which was prepared by the same synthesis protocol as the present study [33]. Compared to the FGnP, whose F has a much higher electronegativity ($\chi_F = 3.98$) and smaller atomic size ($d_F = 72$ pm) than carbon ($\chi_C = 2.55$, $d_C = 77$ pm), SbGnP ($\chi_{Sb} = 2.05$, $d_{Sb} = 141$ pm) showed higher initial Coulombic efficiency and reversible capacity

than FGnP. This was further indication of the stronger effect of the d_M-d_M than χ_M on the anode performance for LIBs.

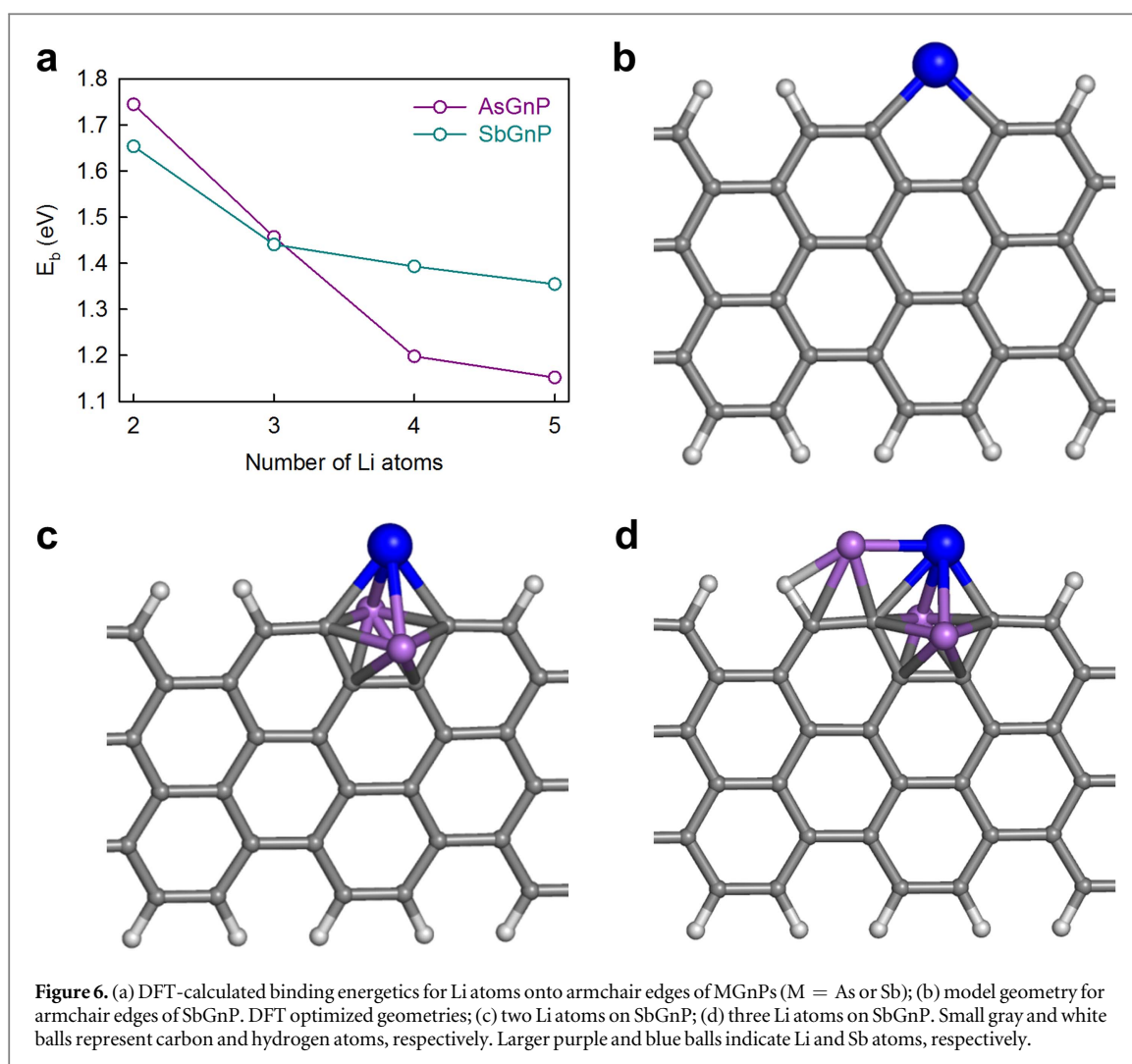
To understand the effect GnPs metalation on Li storage, we performed first-principle DFT calculations for the properties of Li binding to the edges of MGnPs. In a previous study, the binding energies of a Li atom to a single pure graphene surface and to graphite interstitial sites were determined to be about 1.2 eV and 2.0 eV, respectively [61], indicating that the insertion/extraction of lithium ions in graphene was relatively easier. Based on the same computation parameters, it was found that the Li adsorbates interacted with a single pure graphene at the edges with stronger binding energy than at the surface (figure S17).

In our samples, hydrogen passivated graphene edges were selectively decorated by metal atoms with or without oxygenated species, such as C–OH and –COOH functional groups. As expected, the main focus was on the Li binding energetics of the metal-decorated termini, in comparison with the pure graphene surface. Moreover, the functionalized edges of the MGnPs were aggregated into a glassy form, and some part of them interfaced with the electrolyte. To simulate whether the metal-decorated edge can accommodate a higher concentration of Li atoms than the graphite interstitials within the desired window, therefore, we also calculated the binding energetics by increasing the number of Li adsorbates.

For all of the model geometries with oxygen species, Li atoms developed strong Li–O bonds during geometric optimization by DFT total-energy minimization. This indicates that the Li coming to the oxygen sites is vulnerable to the formation of segregated lithium-oxide clusters. However, when the edges were free of oxygen atoms, each metal-decorated site could accommodate 3–4 Li atoms in the desired energy window. Figure 6 presents the Li binding energetics of the As and Sb decorated sites of armchair-type graphene edges (figure 6(a)) and DFT-optimized Sb-decorated edges and its Li-adsorption configurations (figures 6(b)–(d)). The metal-decorated graphene edges without oxygen atoms can lead to a higher Li concentration than for bulk graphite at a binding energy lower than 2.0 eV (figure 6(a)). This is almost consistent with the results of the higher capacity of MGnPs than references CGnP and HGnP, as well as high initial CE for MGnPs with less oxygenated groups at the termini. It should be noted that the slope of the binding energy, as shown in figure 6(a), is slightly milder but similar to that for bulk graphite [61]. In addition, we also performed similar investigation of the Bi-decorated armchair edge, but found that bismuth is easily detached from the graphene edges when three or more Li atoms concentrate at the site. It is thought that the strength of a C–Bi bond is weaker than one between C–As or C–Sb; thus, Li could substitute for Bi, thereby effectively segregating Bi from the active graphene edge. A few other metals with

Table 1. Initial capacity and capacity retention of MGnPs after 500 cycles.

	MGnPs											
	M = Post-transition metal or semimetal										M=C	M=H
	B-family			C-family			N-family			C		
	Al	Ga	In	Ge	Sn	Pb	As	Sb	Bi			
1st cycle (mAh g^{-1})	377	820.9	532.4	1088.5	1234.7	1046.7	1335.3	1212.3	955.8	1260.8	1064.1	
500th cycle (mAh g^{-1})	213.8	183.7	82.8	218	413.9	260	173.8	521.5	402.3	296.5	249.8	
Retention	56.7%	22.4%	15.5%	20%	33.5%	24.8%	13%	43%	42.1%	23.5%	23.5%	



similar configurations are summarized in figure S18. Hence, it could be noted that the optimum atomic size (d_M) of MGnPs is closely related to electrochemical performance of LIBs.

4. Conclusion

We prepared a series of metalated GnPs (MGnPs, $M = \text{Al}, \text{Ga}, \text{In}, \text{Ge}, \text{Sn}, \text{Pb}, \text{As}, \text{Sb}$ or Bi). The metals (M 's, post-transition metals and semimetals) have lower electronegativity (χ , $1.61 \leq \chi_M \leq 2.18$) than carbon ($\chi_C = 2.55$, $d_C = 77$ pm) but much larger atomic size (d , $120 \leq d_M \leq 175$ pm). The experimental results and quantum mechanics calculations clearly revealed that the optimum atomic size (d_M) was more important than electronegativity (χ_M). For example, GaGnP ($\chi_{\text{Ga}} = 1.81$, $d_{\text{Ga}} = 135$ pm), SnGnP ($\chi_{\text{Sn}} = 1.96$, $d_{\text{Sn}} = 140$ pm), and SbGnP ($\chi_{\text{Sb}} = 2.05$, $d_{\text{Sb}} = 141$ pm) exhibited better anode performance in LIBs, due to higher capacity, rate capability, and initial Coulombic efficiency than all the other MGnPs ($M = \text{Al}, \text{In}, \text{Ge}, \text{Pb}, \text{As}$, or Bi) as well as the references HGnP ($\chi_{\text{H}} = 2.20$, $d_{\text{H}} = 37$ pm) and CGnP ($\chi_C = 2.55$, $d_C = 77$ pm). The enhanced

electrochemical performance is mainly attributed to the optimum $d_M \sim 140$ pm, which not only enables efficient electrolyte penetration but also facilitates fast electron and ion transport across the graphitic layers. Moreover, the stronger interaction between lithium ions and MGnPs via Li-M-C, than via Li-MO-C, accommodates greater lithium ion storage and decreases the irreversible reaction between lithium ions and OM (or oxygenated groups) at the active termini, leading to high capacity and high initial Coulombic efficiency, respectively. In addition, given that the use of heteroatom (especially nitrogen)-doped carbon materials in various energy storage fields is of great interest, the strategy for enhancing anode performance by employing MGnPs for LIBs using the positive effect of d_M at their termini, could be widely extended to other energy-related fields.

Acknowledgments

The authors are grateful for financial support from the Creative Research Initiative (CRI, 2014R1A3A2069102), BK21 Plus (10Z20130011057) and Science Research Center (SRC, 2016R1A5A1009405) programs through

the National Research Foundation (NRF) of Korea, as well as from the AFOSR (FA9550-12-1-0037, FA-9550-12-1-0069, FA 9550-10-1-0546), NSF (NSF-CMMI-1000768, NSF-DMR-1106160). Jiantie Xu and In-Yup Jeon contributed equally.

References

- [1] Goodenough J B and Kim Y 2009 *Chem. Mater.* **22** 587–603
- [2] Etacheri V, Marom R, Elazari R, Salitra G and Aurbach D 2011 *Energy Environ. Sci.* **4** 3243–62
- [3] Xu J, Dou S, Liu H and Dai L 2013 *Nano Energy* **2** 439–42
- [4] Goriparti S, Miele E, De Angelis F, Di Fabrizio E, Proietti Zaccaria R and Capiglia C 2014 *J. Power Sources* **257** 421–43
- [5] Yoo E, Kim J, Hosono E, Zhou H-S, Kudo T and Honma I 2008 *Nano Lett.* **8** 2277–82
- [6] Geim A K and Novoselov K S 2007 *Nat. Mater.* **6** 183–91
- [7] Chen Y, Lu Z, Zhou L, Mai Y-W and Huang H 2012 *Energy Environ. Sci.* **5** 7898–902
- [8] Liu F, Song S, Xue D and Zhang H 2012 *Adv. Mater.* **24** 1089–94
- [9] Qie L, Chen W-M, Wang Z-H, Shao Q-G, Li X, Yuan L-X, Hu X-L, Zhang W-X and Huang Y-H 2012 *Adv. Mater.* **24** 2047–50
- [10] Chen Y, Li X, Park K, Song J, Hong J, Zhou L, Mai Y-W, Huang H and Goodenough J B 2013 *J. Am. Chem. Soc.* **135** 16280–3
- [11] Fang Y, Lv Y, Che R, Wu H, Zhang X, Gu D, Zheng G and Zhao D 2013 *J. Am. Chem. Soc.* **135** 1524–30
- [12] Li J, Yao R, Bai J and Cao C 2013 *Chem. Plus. Chem.* **7** 797–800
- [13] Li Z, Xu Z, Tan X, Wang H, Holt C M B, Stephenson T, Olsen B C and Mitlin D 2013 *Energy Environ. Sci.* **6** 871–8
- [14] Wang Z-L, Xu D, Wang H-G, Wu Z and Zhang X-B 2013 *ACS Nano* **7** 2422–30
- [15] Dutta S, Bhaumik A and Wu K C W 2014 *Energy Environ. Sci.* **7** 3574–92
- [16] Mukherjee R, Thomas A V, Datta D, Singh E, Li J, Eksik O, Shenoy V B and Koratkar N 2014 *Nat. Commun.* **5** 3710
- [17] Song H, Li N, Cui H and Wang C 2014 *Nano Energy* **4** 81–7
- [18] Sun H, Xin G, Hu T, Yu M, Shao D, Sun X and Lian J 2014 *Nat. Commun.* **5** 4526
- [19] Yan Y, Yin Y-X, Xin S, Guo Y-G and Wan L-J 2012 *Chem. Commun.* **48** 10663–5
- [20] Fan Z, Yan J, Ning G, Wei T, Zhi L and Wei F 2013 *Carbon* **60** 558–61
- [21] Hassoun J, Bonaccorso F, Agostini M, Angelucci M, Betti M G, Cingolani R, Gemmi M, Mariani C, Panero S and Pellegrini V 2014 *Nano Lett.* **14** 4901–6
- [22] Xu J, Lin Y, Connell J W and Dai L 2015 *Small* **11** 6179–85
- [23] Shin W H, Jeong H M, Kim B G, Kang J K and Choi J W 2012 *Nano Lett.* **12** 2283–8
- [24] Hu C, Wang L, Zhao Y, Ye M, Chen Q, Feng Z and Qu L 2014 *Nanoscale* **6** 8002–9
- [25] Zhan L, Yang S, Wang Y, Wang Y, Ling L and Feng X 2014 *Adv. Mater. Interfaces* **1** 130149
- [26] Hou J, Cao C, Idrees F and Ma X 2015 *ACS Nano* **9** 2556–64
- [27] Xu J, Jeon I Y, Seo J M, Dou S, Dai L and Baek J B 2014 *Adv. Mater.* **26** 7317–23
- [28] Xu J, Shui J, Wang J, Wang M, Liu H, Dou S, Jeon I-Y, Seo J-M, Baek J-B and Dai L 2014 *ACS Nano* **8** 10920–30
- [29] Zheng F, Yang Y and Chen Q 2014 *Nat. Commun.* **5** 5261
- [30] Wu Z-S, Ren W, Xu L, Li F and Cheng H-M 2011 *ACS Nano* **5** 5463–71
- [31] Paraknowitsch J P and Thomas A 2013 *Energy Environ. Sci.* **6** 2839–55
- [32] Wang P, Qiao B, Du Y, Li Y, Zhou X, Dai Z and Bao J 2015 *J. Phys. Chem. C* **119** 21336–44
- [33] Jeon I-Y et al 2015 *Adv. Funct. Mater.* **25** 1170–9
- [34] Xia L, Wang S, Liu G, Ding L, Li D, Wang H and Qiao S 2016 *Small* **12** 853–9
- [35] Dahn J R 1991 *Phys. Rev. B* **44** 9170–7
- [36] Ohzuku T, Iwakoshi Y and Sawai K 1993 *J. Electrochem. Soc.* **140** 2490–8
- [37] Tran T and Kinoshita K 1995 *J. Electrochem. Soc.* **386** 221–4
- [38] Uthaisar C and Barone V 2010 *Nano Lett.* **10** 2838–42
- [39] Jeon I-Y, Choi H-J, Jung S-M, Seo J-M, Kim M-J, Dai L and Baek J-B 2012 *J. Am. Chem. Soc.* **135** 1386–93
- [40] Filella M and May P M 2003 *Geochim. Cosmochim. Acta* **67** 4013–31
- [41] Kresse G and Furthmüller J 1996 *Phys. Rev. B* **54** 11169
- [42] Kresse G and Furthmüller J 1996 *Comput. Mater. Sci.* **6** 15–50
- [43] Kohn W and Sham L J 1965 *Phys. Rev.* **140** A1133
- [44] Perdew J P, Burke K and Ernzerhof M 1996 *Phys. Rev. Lett.* **77** 3865
- [45] Jeon I-Y et al 2015 *Nat. Commun.* **6** 7123
- [46] Ju M J et al 2016 *Sci. Adv.* **2** e1501459
- [47] Jeon I-Y, Shin Y-R, Sohn G-J, Choi H-J, Bae S-Y, Mahmood J, Jung S-M, Seo J-M, Kim M-J and Chang D W 2012 *Proc. Natl Acad. Sci.* **109** 5588–93
- [48] Seo J-M, Jeon I-Y and Baek J-B 2013 *Chem. Sci.* **4** 4273–7
- [49] Jeon I Y, Zhang S, Zhang L, Choi H J, Seo J M, Xia Z, Dai L and Baek J B 2013 *Adv. Mater.* **25** 6138–45
- [50] Chen M, Wang X, Yu Y, Pei Z, Bai X, Sun C, Huang R and Wen L 2000 *Appl. Surf. Sci.* **158** 134–40
- [51] Wolter S, Luther B, Waltemyer D, Önnby C, Mohnhey S and Molnar R 1997 *Appl. Phys. Lett.* **70** 2156–8
- [52] Zheng D, Gao Z, He X, Zhang F and Liu L 2003 *Appl. Surf. Sci.* **211** 24–30
- [53] Molle A, Bhuiyan M N K, Tallarida G and Fanciulli M 2006 *Appl. Phys. Lett.* **89** 083504
- [54] Kwoka M, Ottaviano L, Passacantando M, Santucci S, Czempik G and Szuber J 2005 *Thin Solid Films* **490** 36–42
- [55] Molak A, Talik E, Kruczek M, Paluch M, Ratuszna A and Ujma Z 2006 *Mater. Sci. Eng. B* **128** 16–24
- [56] Zhou W, Kibler L and Kolb D 2004 *Electrochim. Acta* **49** 5007–12
- [57] Schmidt T, Grgur B, Behm R, Markovic N and Ross P Jr 2000 *Phys. Chem. Chem. Phys.* **2** 4379–86
- [58] Goldstein J, Newbury D E, Echlin P, Joy D C, Romig A D Jr, Lyman C E, Fiori C and Lifshin E 2012 *Scanning Electron Microscopy and X-Ray Microanalysis: a Text for Biologists, Materials Scientists, and Geologists* (New York: Springer)
- [59] Carlson T 2013 *Photoelectron and Auger Spectroscopy* (New York: Springer)
- [60] Fergus J W 2010 *J. Power Sources* **195** 939–54
- [61] Odkhuu D, Jung D H, Lee H, Han S S, Choi S-H, Ruoff R S and Park N 2014 *Carbon* **66** 39–47